

CAMELOT

UNDERSTANDING CHARGE, MASS AND HEAT TRANSFER IN FUEL CELLS FOR TRANSPORT APPLICATIONS

Grant agreement no.: 875155
Start date: 01.01.2020 – Duration: 36 months
Project Coordinator: Patrick Fortin - SINTEF

DELIVERABLE REPORT

D2.2 – IMPLEMENTED AND VALIDATED MODEL OF LIQ. WATER TRANSPORT FOR ULTRA THIN MEAS		
Due Date	M36	
Author (s)	David Harvey and Jiri Hrdlicka	
Workpackage	2	
Workpackage Leader	David Harvey	
Lead Beneficiary	FAST Simulations	
Date released by WP leader	18/02/2024	
Date released by Coordinator	20/02/2024	
DISSEMINATION LEVEL		
PU	Public	X
PP	Restricted to other programme participants (including the Commission Services)	
RE	Restricted to a group specified by the consortium (including the Commission Services)	
CO	Confidential, only for members of the consortium (including the Commission Services)	
NATURE OF THE DELIVERABLE		
R	Report	X
P	Prototype	
D	Demonstrator	
O	Other	

SUMMARY	
Keywords	<i>Liquid water model, water transport, PEMFC, Performance</i>
Abstract	<i>An overview of an original saturation driven liquid water model is given and discussed. The broader equations which govern transport in a pemfc performance model are presented and further improvements made upon on a previous integration of a dissolved water uptake model are provided. The updated liquid water transport model implemented to replace the saturation-driven original approach is given, with a review of the input criterion, key characteristic data, and an overview of the MEA level predictions. The performance model predictions are compared with a set of data representing Hot & Dry and Cold & Wet performance to establish a baseline validation.</i>
Public abstract for confidential deliverables	

REVISIONS			
Version	Date	Changed by	Comments
1	Dec 30 2023	David Harvey	Draft
2	Dec 30 2024	David Harvey	Updates to descriptions
3	Feb 17 2024	Jiri Hrdlicka	Added thin ionomer model updates
4	Feb 17 2024	David Harvey	Corrected plots
4	Feb 18 2024	David Harvey	Release

WATER TRANSPORT IN THIN IONOMERIC MATERIALS AND MEMBRANES

CONTENT

1	Executive Summary.....	4
2	Introduction	4
3	Scope.....	8
4	Discussion	9
4.1	Model Improvements and Rebuild.....	9
5	Verification and Validation	18
6	Conclusions and future work	21
7	References	21

1 EXECUTIVE SUMMARY

FAST-FC was originally developed using a saturation-driven liquid water transport approach and combined with a superimposed membrane RH method that assumed quick equilibrium with the surrounding gas mixture for water uptake. In this project, it was the intent to improve the saturation-driven liquid water transport approach by replacing it with a liquid-pressure driven transport approach and to integrate a full dissolved liquid water transport model which has the capability to capture the behaviour of thin membranes. In this report, the replacement of the original saturation-driven liquid water is discussed, and a liquid-pressure driven formulation is proposed. Further, discussion of the relationship between the capillary pressure vs saturation is discussed in the light of measurements on fuel cell media which have been incorporated. Lastly, the replacement of the liquid water transport model has allowed for further improvements in the dissolved water uptake based on a new method for switching between the driving force directions.

2 INTRODUCTION

Liquid water transport models have been developed by many groups with the intent to describe the effect of liquid water on the performance of PEM fuel cells. In literature the predominant descriptions are either saturation driven, or liquid water pressure driven, with the bulk largely being those in the saturation-driven methodology. As part of the original development of FAST-FC, a saturation-driven methodology was used, and it is a good starting point to revisit the layout as the groundwork to discuss the shift to an improved methodology.

The saturation-driven liquid water transport model is based on the multi-phase mixture model introduced by Wang et al. in 1996. In that work, the mass conservation equation for liquid water was described according to (Wang & Cheng, 1996):

$$\frac{\partial(\rho_l v_l)}{\partial t} + \nabla \cdot (\rho_l \vec{u}_l) = S_l$$

where, v_l is the volume fraction of the pore space that is occupied by liquid water, ρ_l is the density of liquid water, \vec{u}_l is the velocity of the liquid water phase, S_l is the mass source or sink of liquid water.

The velocity of the liquid water phase can be described using the generalized Darcy's law:

$$\vec{u}_l = -\frac{k_l}{\mu_l} \nabla p_l$$

From this, the governing form of the mass conservation for liquid water becomes:

$$\frac{\partial(\rho_l v_l)}{\partial t} - \nabla \cdot \left(\frac{\rho_l k_l}{\mu_l} \nabla p_l \right) = S_l$$

It is at this point that the equation can be recast in terms of saturation, and this is done by considering a definition for the gradient in the liquid water pressure.

Within the porous media of a fuel cell, there will exist interfaces within the various pores where the air and liquid phases meet. At these interfaces there will exist discontinuities in the pressure between the gas phase and the liquid phase; the magnitude of this discontinuity is a function of the curvature of that interface. Across this interface, the difference in pressure is described as the capillary pressure and it is generally written as the difference between the non-wetting phase and wetting phase (with respect to the pore) (Bear, 1988):

$$p_c = p_{nw} - p_w$$

In the consideration of the scenario within fuel cell porous media, the gas will be the wetting phase and the liquid water the non-wetting phase; such that the capillary pressure equation becomes:

$$p_c = p_l - p_g$$

Re-arrangement and substitution of this into the mass conservation equation yields:

$$\frac{\partial(\rho_l v_l)}{\partial t} - \nabla \cdot \left(\frac{\rho_l k_l}{\mu_l} (\nabla p_g - \nabla p_c) \right) = S_l$$

However, the mass conservation equation is still not in its desired form as it is expressed in terms of the gradient of the gas pressure, which itself is solved through the gas phase mass conservation equation, and the gradient in capillary pressure. To move further, some further relationships are needed with respect to the capillary pressure; the capillary pressure is generally agreed to be related to the water content, or saturation, of the pore space and as such the gradient in capillary pressure could be re-written in terms of this (Udell, 1985).

$$J(s) = \frac{p_c}{\sigma \cos \theta_c} \left(\frac{k_{dry}}{v_{pore}} \right)$$

where, σ is the surface tension, θ_c is the contact angle, k_{dry} is the dry permeability or absolute permeability of the media, and v_{pore} is the volume fraction of the gas/open pores.

The relationship between capillary pressure and saturation was the topic of heat transfer studies in porous media as far back as Udell (Udell, 1985); Udell implemented the use of the Leverett-J function and this was adopted by Wang and Cheng (Wang & Cheng, 1996) in their multiphase mixture model approach for PEMFCs. Other approaches have studied the relationship between the saturation and capillary pressure parametrically (Nastarajan & Nguyen, 2001) while others have implemented alternative empirical (Vetter & Schumacher, Free open reference implementation of a two-phase pem fuel cell model, 2019) or semi-empirical (Dujc, et al., 2018) relationships. By far the majority of publications have employed the Leverett-J function (Wang & Cheng, 1996) (Udell, 1985) (Wang & Wang, 2006) (Shah, Kim, Sui, & Harvey, 2007) (Shah, Kim, Sui, & Harvey, 2007) (Das, Li, & Liu, 2010) (Harvey, 2017). The Leverett-J function originated from a study on consolidated sands in the field of reservoir engineering (Leverett, 1942); while it is the most common relationship used to describe capillary pressure vs. saturation, it does not directly follow that the porous media used in fuel cells exhibits similar behaviors to consolidated sands; nonetheless, as a starting point, the Leverett-J function is commonly reported as:

$$J(s) = \begin{cases} 1.417(1-s) - 2.120(1-s)^2 + 1.263(1-s)^3, & \theta_c < 90^\circ \\ 1.417s - 2.120s^2 + 1.263s^3, & \theta_c \geq 90^\circ \end{cases}$$

The form of the Leverett-J relationship can be re-arranged to solve for capillary pressure,

$$p_c = \left(\frac{v_{pore}}{k_l} \right) \sigma \cos(\theta_c) J(s)$$

From this, the capillary pressure vs. saturation relationship has the form as shown in Figure 1. Figure 2 shows the effect of the contact angle based on imbibition or an advancing non-wetting phase which is displacing the wetting phase (this is true of a hydrophobic media).

In order to complete the implementation of the saturation-driven liquid water transport equation, the gradient in capillary pressure can be recast in order to achieve the inclusion of the saturation as the solved variable:

$$\frac{\partial p_c}{\partial x_i} = \frac{\partial p_c}{\partial s} \frac{\partial s}{\partial x_i}$$

where, x_i is representing the spatial directions.

Using this form and substituting it into the mass conversation equation for liquid water, the equation can be recast to solve for the saturation of the media.

$$(\rho_l v_{pore}) \frac{\partial s}{\partial t} - \nabla \cdot \left(\frac{\rho_l k_l}{\mu_l} \frac{\partial p_g}{\partial x_i} - \frac{\rho_l k_l}{\mu_l} \frac{\partial p_c}{\partial s} \frac{\partial s}{\partial x_i} \right) = S_l$$

This form takes on the solved variable as the saturation and the differentiation of the capillary pressure with respect to the saturation becomes the one of the characteristic transport parameters which then embodies the surface tension, absolute/dry permeability, porosity, and contact angle as physical characteristics.

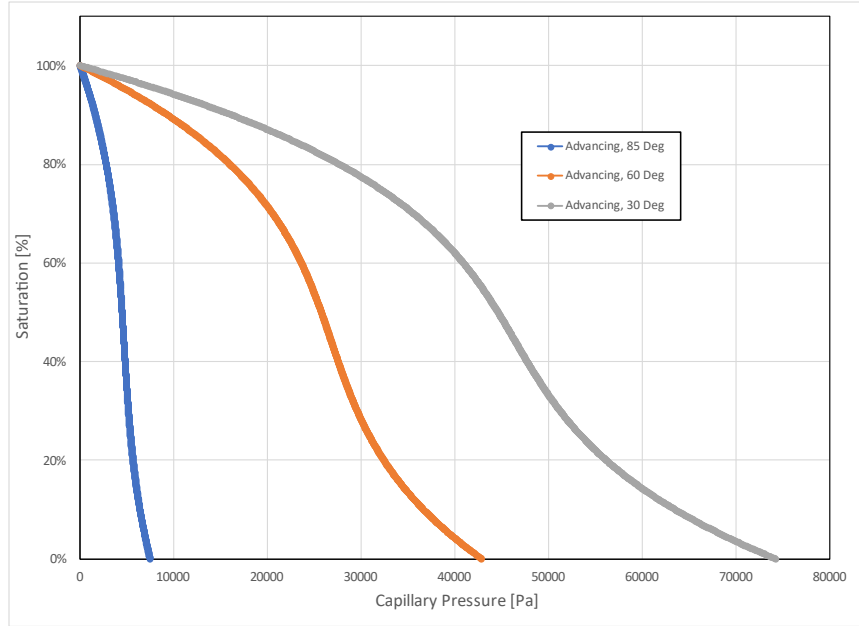


Figure 1: Saturation vs. Capillary Pressure Relationship based on the Leverett-J Function

The permeability for liquid water, k_l , is determined using a relationship between the local saturation and the absolute or dry permeability, k_{dry} , as originally reported by (Udell, 1985) and also applied by (Shah, Kim, Sui, & Harvey, 2007) (Das, Li, & Liu, 2010):

$$k_l = k_{dry} S^3$$

The source term, S_l , for the equation encompasses phase change between the liquid and vapor phases as well, exchange between the liquid and dissolved water phases, and the production of water from the electrochemical reaction (the latter depending on the assumption of in what phase the electrochemical product water is produced, namely the vapor phase, liquid phase, or dissolved phase):

$$S_l = S_{vl}^{ce} + S_{dl}^{ad} + S_l^{rxn}$$

where the superscripts, ce , ad , and rxn , denote condensation-evaporation, adsorption-desorption and the electrochemical reaction, respectively and the subscript vl and dl denote the transfer between the vapor and liquid phases and the dissolved and liquid phases, respectively. It is noted that the term S_{vl}^{ce} applies in all the porous media whereas the term S_{dl}^{ad} applies only within the anode and cathode catalyst layers.

The source term for the production of water resulting from electrochemical reactions follows that this applied to the ORR reaction on the cathode and is of a similar form to that reported by others (Das, Li, & Liu, 2010) (Harvey, 2017) (Shah, Kim, Sui, & Harvey, 2007).

With respect to the source terms related to the condensation and evaporation, the terms address the exchange between the phases but also the numerical complexity of the implementation by applying a switching term approach in order to respect both the driving force of the exchange but also a form that can be implemented with a sufficient level of numerical stability.

The phase change between the liquid and vapor phases must respect the fact that there can be no evaporation when liquid water is not present but also that there cannot be condensation when the pore volume is completely saturated. The driving force for both equations is the departure from the “equilibrium” local relative humidity (RH) such that a local relative humidity in excess of the “equilibrium” RH should produce a condensation driving force and a local value of RH lower than the “equilibrium” RH should produce an evaporation driving force provided that the local saturation is non-zero.

The source term, S_{vl}^{ce} , can be written as:

$$S_{vl}^{ce} = M_{w,H_2O} h_{vl}^{ce} (p_g x_{H_2O} - p_{H_2O}^{sat})$$

With, M_{w,H_2O} as the molecular weight of water, h_{vl}^{ce} as the rate of exchange between the vapor and liquid phases due to condensation and evaporation, x_{H_2O} is the mole fraction water vapor in the local gas mixture, and $p_{H_2O}^{sat}$ is the local saturation pressure of vapor water (“equilibrium” saturation pressure).

Of note with this equation is that the term is written with respect to the liquid phase set that a local vapor pressure higher than the saturation pressure will produce a positive source term and thus an increase in the mass of liquid water (condensation) and a local vapor pressure below the saturation pressure will produce a negative source term and thus a decrease in the mass of liquid water (evaporation).

The rate of exchange between the vapor and liquid phases due to condensation and evaporation, h_{vl}^{ce} , is written to incorporate a switching behaviour to capture the transition between scenarios where condensation is “on” and evaporation is “off” and vice versa. The term, h_{vl}^{ce} , is written as:

$$h_{vl}^{ce} = h_{vl}^c + h_{vl}^e$$

Where, h_{vl}^c is:

$$h_{vl}^c = \frac{k_c v_{pore} (1-s) x_{H_2O}}{2R_g T} \left(1 + \frac{|p_g x_{H_2O} - p_{H_2O}^{sat}|}{p_g x_{H_2O} - p_{H_2O}^{sat}} \right)$$

and,

$$h_{vl}^e = \frac{k_e v_{pore} s \rho_l}{2M_{w,H_2O}} \left(1 - \frac{|p_g x_{H_2O} - p_{H_2O}^{sat}|}{p_g x_{H_2O} - p_{H_2O}^{sat}} \right)$$

Numerically, this creates a switching behaviour that allows the transition between scenarios of evaporation and condensation, however there are numerical instabilities that can occur in scenarios such as when the RH reaches 100% locally as the definition for each of the individual evaporation and condensation rates becomes undefined. This will be addressed in the revised model which is the subject of this work.

The exchange between the liquid phase and dissolved phase has been discussed in the context of the deliverable report 2.1 and will be present in the later section related to the improved liquid water transport model. In the original model, pre-Camelot, the water uptake into the ionomer was largely disabled due to stability issues and as such the membrane water content was estimated based on the local RH and assumption of equilibrium between the ionomer and the local gas humidity.

Using the original model formulations, as shown above, the predictions of local water content within the cathode (catalyst and GDL) are shown in Figure 2 and Figure 3. From these two figures, all the input parameters are constant with the only change related to the contact angle between the porous media and the non-wetting phase (liquid water). The difference in predicted water content is significant and does not correspond to a large change in performance. This is, in essence, the critique of these models in that the inputs are so empirically driven and, to a large extent, the models are not validated heavily against ex-situ experimental data for either mercury or water intrusion for the fuel cell media.

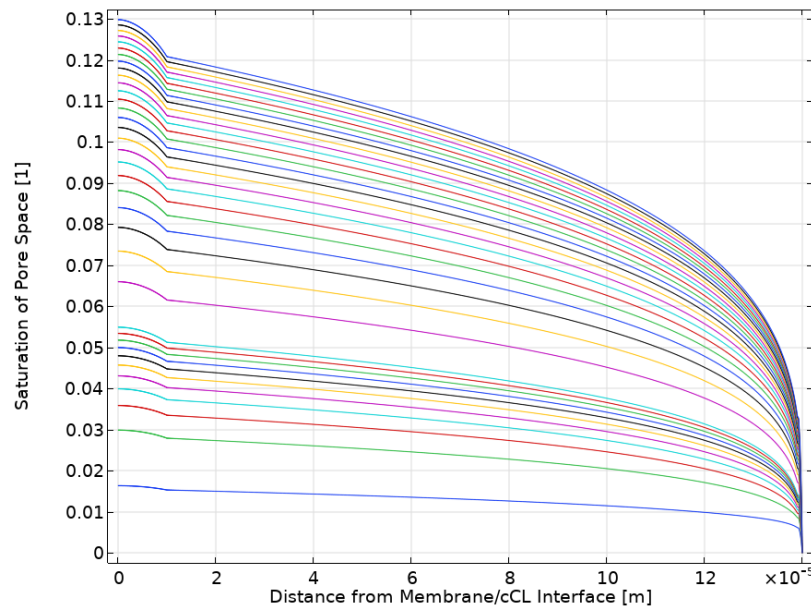


Figure 2: Local saturation predicted in the cathode electrode for an advancing non-wetting phase (89 degrees) with RH=100% (Increasing saturation corresponds to increasing operating current density).

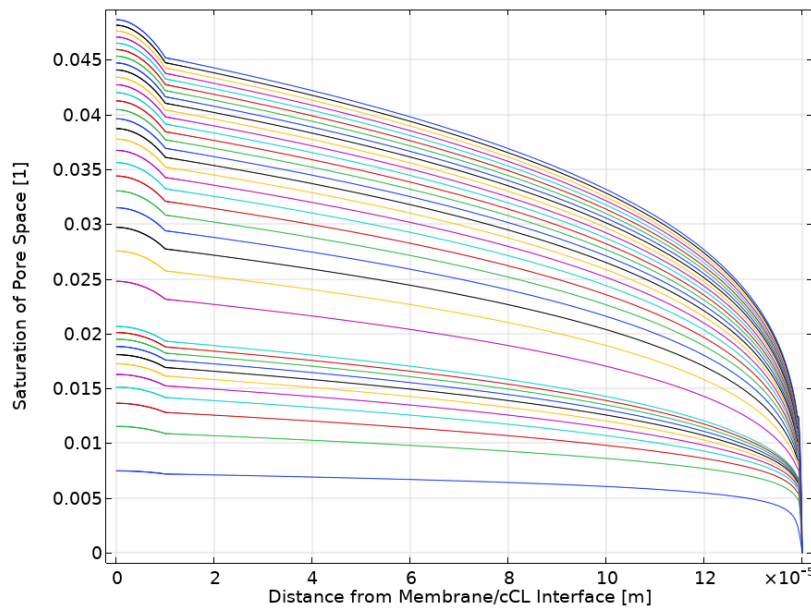


Figure 3: Local saturation predicted in the cathode electrode for an advancing non-wetting phase (45 degrees) with RH=100% (Increasing saturation corresponds to increasing operating current density).

Up to this point the model within FAST-FC has largely been based on a fitted approach carried out against the data generated in a previous project in 2014. This work was based on sub-model relationships for properties which were determined using microstructural models as reported in (Harvey, 2017).

3 SCOPE

The development and improvements in this report are constrained to steady-state and performance of a PEMFC model. The report provides an overview with the main improvements but does not cover a full in-depth build-up of the model physics, for more information on topics not covered here the readers can be referred to other pre-existing documents related to FAST-FC upon which the work in this project is building.

4 DISCUSSION

4.1 Model Improvements and Rebuild

As part of the implementation of an improved liquid water transport model, the model was re-built from the ground up. This was done to ensure that all of the variables and equations implemented were re-structured into both a format that was simpler from a user experience perspective but also to ensure that the implementation was achieved consistently without background convolution with previous approaches. For this reason, this section will layout the model largely from scratch in order to provide a complete, albeit concise, overview of the full implementation.

In proceeding with the ground-up rebuild, the model was restructured first into a single phase, non-isothermal baseline including the revised dissolved water transport model and then extended into a two-phase, non-isothermal incorporating both the revised dissolved water transport and the improved liquid water transport sub-models.

4.1.1 Single Phase

4.1.1.1 Electron Transport

Electron transport within the porous media (diffusion media, catalyst layers, and bipolar plates, the latter in the case of the 2D implementation) is described using Ohm's law:

$$\nabla \cdot (\sigma_e^{eff} \nabla \phi_e) = S_e$$

Where the source term, S_e , is active within the anode and cathode catalyst layers. Specifically, the source term is equal to the electrochemical reaction source term, S_i , which is determined using either the Tafel-Heyrovski-Volmer description for the Anode HOR reaction or a modified form an agglomerate based-Butler Volmer formulation for the Cathode ORR reaction. Both descriptions, the Anode THV HOR and the agglomerate-based Butler Volmer, can be found in (Harvey, 2017).

4.1.1.2 Proton Transport

Proton transport within the anode catalyst, cathode catalyst, and polymer membrane is, similarly to electron transport, also described using Ohm's law:

$$-\nabla \cdot (\sigma_p^{eff} \nabla \phi_p) = S_p$$

The source term, S_p , is also determined from S_i based on the electrochemical models found in (Harvey, 2017) for the ORR and HOR reactions.

The nomenclature for the protons is that they flow in the direction of lower potential (ie from Anode to Cathode) whereas the electrons in the direction of higher potential (ie from the Anode to the Cathode). In describing both charge transport equations in this manner, the driving force, namely the activation overpotential, takes on a form in which is drives the correct directionality (anode reaction proceeding in a net anodic direction and cathode reaction proceeding in a net cathodic direction) organically.

4.1.1.3 Species Transport

The species transport within the model is written on a mass basis and includes transport both due to diffusion but also convection such that the governing equation has the following form:

$$\nabla \cdot (-\rho_{mix} D_{i,mix}^{eff} \nabla w_i + \rho_{mix} \vec{v}_{avg}) = S_{mass,i}$$

Where, w_i , is the mass fraction, ρ_{mix} is the mixture density, $D_{i,mix}^{eff}$ is the effective diffusivity of species i into the mixture, \vec{v}_{avg} is the local mixture average velocity, and $S_{mass,i}$ is the source of mass of species i .

The sources of mass for the oxygen and hydrogen species exist within the catalyst layers and arise due to electrochemical reactions. Whereas the sources of mass for water arise due to production from the ORR in the cathode catalyst layer but also exists in the porous transport layers and the anode catalyst layer due to water adsorption and desorption into the ionomer.

4.1.1.4 Dissolved Water Transport

During the second reporting period, a mathematical description of water transport based on the chemical potential leaned on two concepts: 1) the ionomer is a mixture of the dissolved water and the polymer matrix and 2) the chemical potential in any water phase is derived from a single reference defined at the triple point of water.

When dealing with water in a single phase, the reference value of the chemical potential can be set to zero for simplicity. In multi-phase scenarios, it is necessary to derive all values from a single reference to maintain consistency. The triple point of water ($p^t = 611 \text{ Pa}$, $T^t = 273.16 \text{ K}$) is the international convention and under these conditions the chemical potential of vapor, liquid water and ice attain the same value of $\mu_w^t = 0 \text{ J/mol}$ (Wagner & Pruß, 2002).

The variation of the chemical potential of the water with temperature T and pressure p is described by:

$$\mu_w = \mu_w^t + v_w dp - s_{w,m} dT$$

with the reference chemical potential at triple point, μ_w^t , the molar volume of water, v_w , and the molar entropy of water, $s_{w,m}$, can be used to arrive at more convenient reference values in each present phase (Atkins & Paula, 2010, 9th edition). A literature review yields, for example, $\mu_{w,ref}^g = -237.08 \text{ kJ/mol}$ and $\mu_{w,ref}^l = -240.33 \text{ kJ/mol}$ (Adachi, et al., 2010). Such a choice would, however, cause liquid water to be pulled into regions with vapor, contradicting processes seen in nature. To resolve the discrepancy, a fundamental equation of state explicit in the Helmholtz free energy, f , adopted by IAPWS, experimentally validated and valid across the entire range of conditions pertinent to PEM fuel cells (Wagner & Pruß, 2002) has been implemented in GNU/Octave.

T (K)	p (kPa)	a ()	p_{sat} (Pa)	ρ_w^l (kg/m ³)	$\mu_{w,ref}^l$ (J/mol)	ρ_w^g (kg/m ³)	$\mu_{w,ref}^g$ (J/mol)
303.15	100	1.0	4246.92	995.649	-118.3979	0.03041	-120.1606
333.15			19947.38	983.195	-462.6956	0.13043	-464.0318
353.15			47415.78	971.790	-806.6167	0.29368	-807.5111

The computed reference values for liquid and saturated vapor under the same conditions are different, the chemical potential of liquid is higher and would produce transport processes as expected. The authors do not state that such discrepancy results from the approximation error. If genuine, the difference between the chemical potential of vapor and liquid under the same conditions could explain part of the Schröder paradox. At saturation, vapor and liquid exhibit the water activity of one and replacing one phase with the other should result in an additional influx of water into an ionomer.

For vapor equilibration, the chemical potential of the dissolved water follows the Raoult law:

$$\mu_w^d = \mu_{w,ref}^l + RT \ln(x_w^d)$$

Where x_w^d is the mole fraction of the dissolved water. The Raoult law describes the ideal mixing of liquids (Atkins & Paula, 2010, 9th edition) and one can include the interactions between the polymer matrix and the dissolved water using:

$$\mu_w^d = \mu_{w,ref}^l + RT \ln(a_w^d) = \mu_{w,ref}^l + RT \ln(x_w^d) + n_M \frac{\partial \mu_M}{\partial n_w} = \mu_{w,ref}^l + RT \ln(x_w^d) + RT \ln(\gamma_w^d)$$

Where the activity coefficient of the dissolved water, γ_w^d , represents the non-idealities.

The derivation of the formula for the chemical potential of the matrix was not possible with the available data; however, the framework of the chemical potentials allows us to derive the properties of μ_M and their change with the amount of dissolved water:

$$\mu_M = \mu_{M,ref} + \frac{RT}{n_M} \int \ln(\gamma_w^d) dn_w$$

The equilibration with vapor yields

$$\gamma_w^d = \frac{RH}{x_w^d} \exp\left(\frac{\mu_{w,ref}^g - \mu_{w,ref}^l}{RT}\right)$$

Whereas the liquid equilibration reduces to

$$\gamma_w^d = 1/x_w^d$$

Unfortunately, a mechanistic description resulting in a first-principle-based formula has not been found. In single-phase scenarios, one can fit the experimental data recorded using dynamic vapor sorption, but such fit does not offer any improvement or benefit over mathematical descriptions relying on λ , the molar concentration of water, or another equivalent quantity. It can be argued that all such metrics could be used interchangeably, based on which simplifies the rest of the mathematical model most.

In order to incorporate the ionomer model into a full-fledged fuel cell model, molar concentration of the dissolved water in the ionomer, $c_{H_2O}^d$, has been chosen as was most compatible across the rest of the governing equations.

The final form of that improvement adopted a more conventional one but was combined with an improved description and stability improvements around the water adsorption and desorption mechanisms. From this, the governing form of dissolved water transport is:

$$\nabla \cdot \left(-D_{H_2O,ion}^{eff} M_{w,H_2O} \nabla C_{H_2O}^d - \frac{M_{w,H_2O} N_{drag} \sigma_p^{eff} \nabla \phi_p}{\nu_{SO_3^-} F} C_{H_2O}^d \right) = S_{mass,dv}$$

Where, $D_{H_2O,ion}^{eff}$ is the diffusivity of water in the ionomer and was determined using the form reported in (Motupally, Becker, & Weidner, 2000), N_{drag} is the electro-osmotic drag coefficient, σ_p^{eff} is the protonic conductivity, and $\nabla \phi_p$ is the gradient in the proton potential.

The diffusivity of water in the ionomer, according to that reported by Motupally et al., is itself dependent on the water content, such that there is a spike in the transport around a water content of 3:

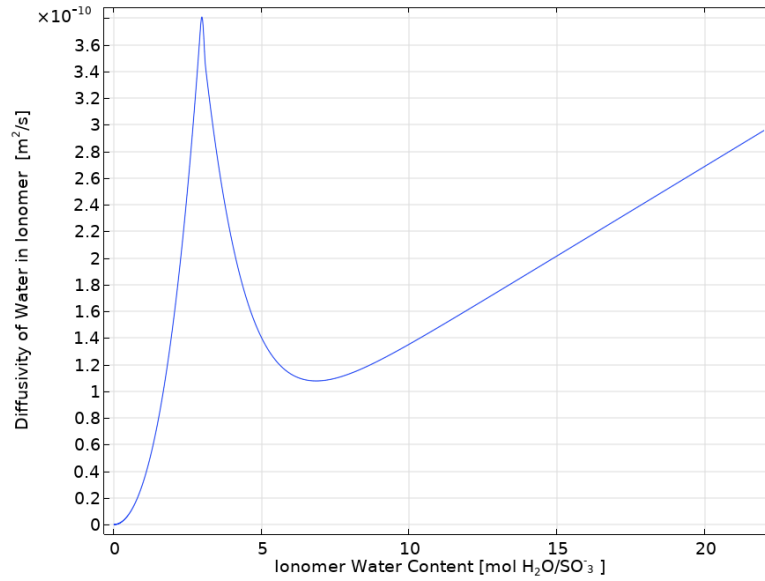


Figure 4: Diffusivity of Water in Ionomer

The value of the hydration number, λ , could be obtained by fitting the dynamic vapor sorption with a cubic polynomial, providing a reasonable accuracy. However, early measurements as well as literature data implied the possibility of temperature dependence. After testing a wide array of sorption models, including sets of implicit equations, the Takata isotherm was chosen as it is mechanistic, includes temperature dependence, includes equivalent weight and is explicit (supplying relative humidity and temperature into the formula gives λ). The Takata isotherm (Takata, Mizuno, Nishikawa, Fukada, & Yoshitake, 2007) has been introduced in D2.1. Here we are updating the formula to provide a candidate showing the best match to 10 and 15 μm samples:

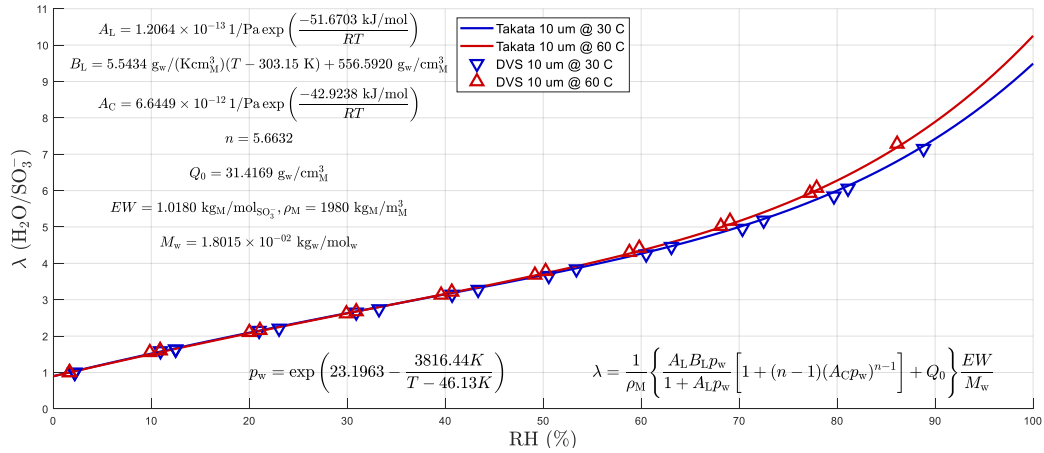


Figure 5: Takata's Isotherm For 10 um CAMELOT Membranes

The value of the electro-osmotic drag has been reported as early as (Springer, Zawodinski, & Gottesfield., 1991) and work by (Ge, Yi, & Ming, 2006) further confirmed the approach that the electro-osmotic drag is a function of the water content but also added that the electro-osmotic drag included a temperature dependence. The latter remains to be added as the data is still not entirely clear as to the form of the relationship and its applicability across a wide range of dissolved water content. Based on this the applied form of the electro-osmotic drag coefficient is:

$$N_d = \frac{2.5}{22} \lambda$$

Noting here that the drag coefficient is unitless and implies that the values of 2.5/22 have representative units which should not be neglected when re-arranging or re-deriving the equations.

$v_{SO_3^-}$ is the fixed charge site concentration which is the moles of sulfonic acid sites per m^3 . This can be determined from the density of the ionomer and the equivalent weight.

The uptake of water from the pores into the dissolved phase is accounted for in the source term, $S_{mass,dv}$, which includes adsorption and desorption from both the vapor (and subsequently) liquid phases.

The source term, $S_{mass,dv}$, must have a unified form within a steady-state implementation and as such this is one of the general areas of instability that usually arises within model frameworks (and FAST-FC is not an exception to this).

$$S_{mass,dv} = M_{w,H_2O} k_{dv} (C_{H_2O}^D - C_{H_2O}^{d,eq})$$

Where k_{dv} is the rate of exchange between the vapor and the dissolved phases and it is a combination of the rate for adsorption and the rate for desorption:

$$k_{dv} = k_{dv}^{ads} + k_{dv}^{des}$$

k_{dv}^{ads} and k_{dv}^{des} are the rates of adsorption and desorption respectively. The terms are in most other works activated and deactivated using switching terms that are related to the driving force, namely, $(C_{H_2O}^D - C_{H_2O}^{d,eq})$ such as:

$$\Gamma_{ads} = 1 + \frac{(C_{H_2O}^{D,eq} - C_{H_2O}^d)}{|(C_{H_2O}^{D,eq} - C_{H_2O}^d)|}$$

In this example, when the dissolved water content is less than the equilibrium level of water content which could be achieved, the value of the fraction becomes “+1” and the overall term, Γ_{ads} , takes on a value of 2. Conversely, when the dissolved water content is greater than the equilibrium level of water content which could be achieved, the value of the fraction becomes “-1” and the overall term, Γ_{ads} , take on a value of 0.

In this way, the use of switching terms can be used to turn on and off the adsorption and desorption processes based on the driving force. However, a point of stability arises when the dissolved water content reaches the equilibrium water content value yielding an indeterminate fraction.

To address this, a different form of the switching behaviour has been implemented using Heaviside functions such that the value of Γ_{ads} and, the pairing term, Γ_{des} are as follows:

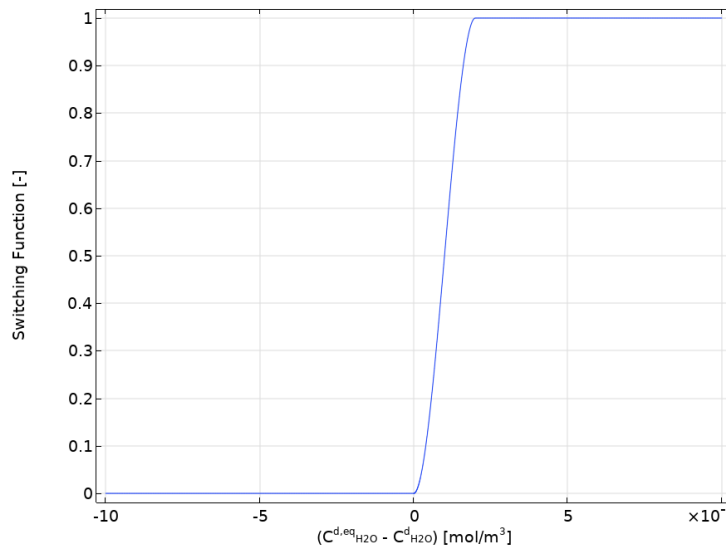


Figure 6: Dissolved-Vapor Water Adsorption Switch

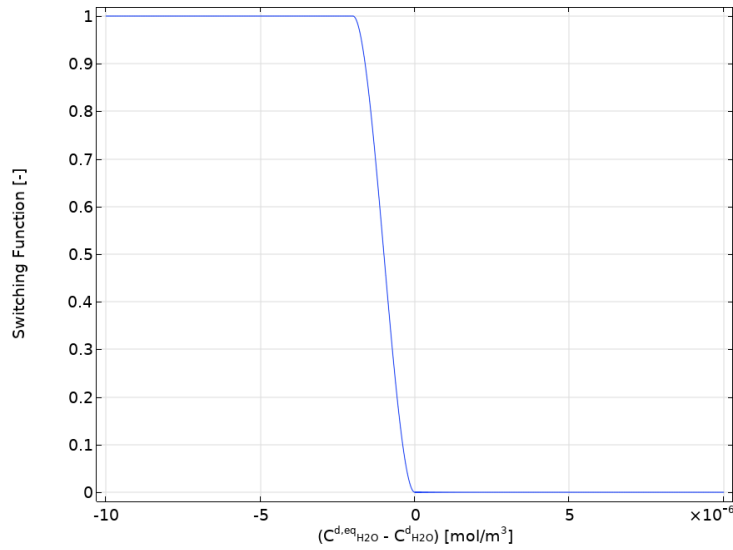


Figure 7: Dissolved-Vapor Water Desorption Switch

These two switches are then applied to the equation for k_{dv} which becomes:

$$k_{dv} = k_{dv}^{ads} \Gamma_{ads} + k_{dv}^{des} \Gamma_{des}$$

The behaviour of k_{dv} then becomes one in which when the dissolved water content is less than the equilibrium value, the value becomes k_{dv}^{ads} and vice versa becoming k_{dv}^{des} when dissolved water content is greater than the equilibrium value. Addressing the previous issue related to the point at which the mass exchange would be in “equilibrium”, both rates are equal to zero when the dissolved water content equals the equilibrium water content.

Using this method, the shape of the water content across the ionomer in the catalyst layers and the ionomer in the membrane appears as follows:

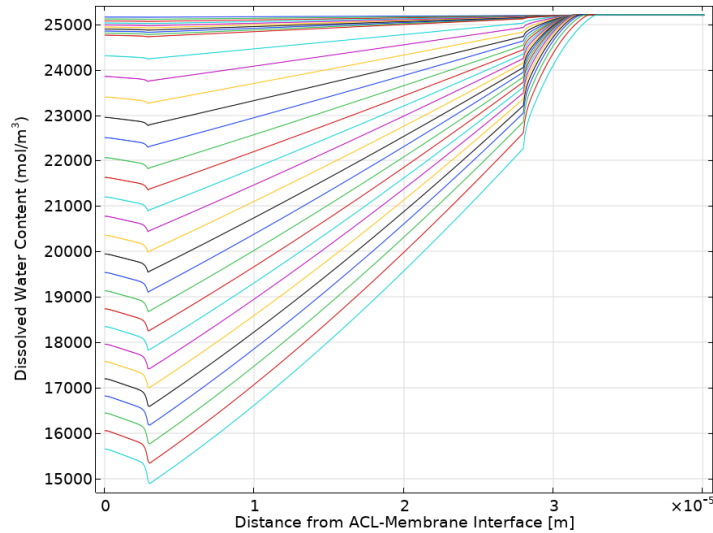


Figure 8: Dissolved water content of the ionomer phase (Anode/Cathode RH 100%, Temperature 80 C)

From Figure 8, the anode catalyst layers are on the left and the depletion of the water content of the anode ionomer can clearly be observed. This effect is due to the severity of the water flux which arises due to electro-osmotic drag. The curves of dissolved water content can be seen in the figure to decline which operating current density and this clearly highlights the severity of the water drag on the anode water content. This drop in water content directly affects the local proton conductivity and results in a higher amount of voltage losses due to the decrease in proton conductivity.

4.1.1.5 Heat Transport

Heat transport in the model is governed by Fourier’s Law and can be written as:

$$-\nabla \cdot (k_T^{eff} \nabla T) = S_{heat}$$

The thermal conductivity is k_T^{eff} which is determined using effective medium theory or specific measured values, where appropriate. The source term for heat production, S_{heat} , includes terms for the heat release due to the electrochemical reactions (specifically the ORR), ohmic heating due to protons, and electrons, and due to water adsorption/desorption from the vapor phase to the dissolved phase.

The application of the heat transport equation yields a conduction of heat throughout the MEA such that a typical profile across the MEA appears as:

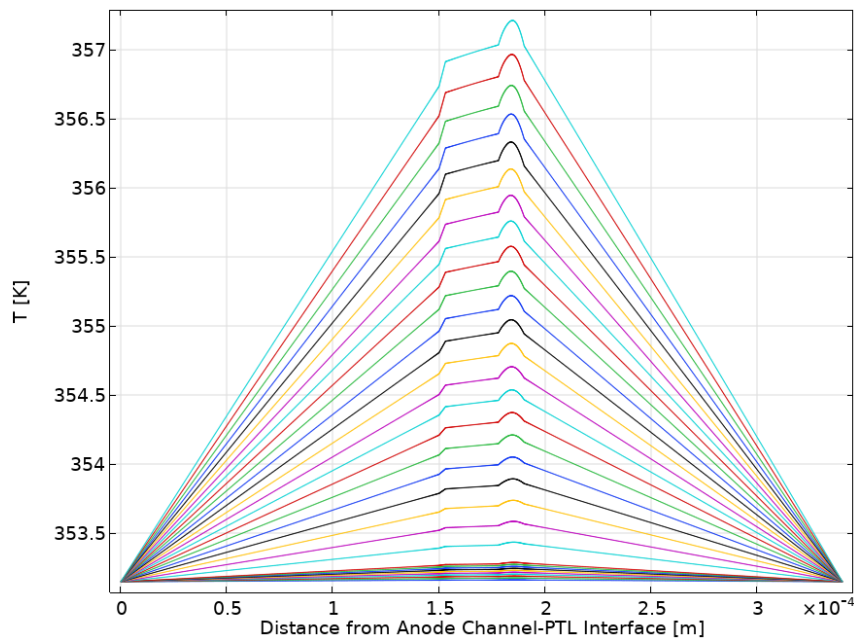


Figure 9: Temperature distribution across the MEA.

From Figure 9, the point of maximum temperature can be seen to occur within the cathode catalyst layers and the temperature shows a linear slope across the membrane to the left toward the anode. This demonstrates that heat flux is occurring from the cathode catalyst layer crossing the membrane towards the anode and across the cathode porous transport layer; with both fluxes going outward towards the cooling channels which are located adjacent to the anode channel on the left and cathode channel on the right.

4.1.2 Improved Two Phase Liquid Water Saturation Model

4.1.2.1 Liquid Water Transport Equation

In the early section the original liquid water transport model was described and had a transport equation which was written as:

$$-\nabla \cdot \left(\frac{\rho_l k_l}{\mu_l} (\nabla p_g - \nabla p_c) \right) = S_l$$

From this form, the original driving force was the gradient in liquid pressure which was replaced using a re-arrangement of the definition for the capillary pressure, p_c :

$$p_c = p_{nw} - p_w$$

This re-arrangement is done in order to “unlock” the use of the Leverett-J function which was one of the only saturation-capillary pressure relationships integrated into early fuel cell models.

In recent years, more characterization studies have been undertaken on the porous transport layers. Specifically, these have been done with a view in understanding the capillary pressure vs saturation (Gostick, Ioannidis, Fowler, & Pritzker, 2009), wettability (Weber A. Z., 2010), effect of saturation on diffusivity (Hwang & Weber, 2012), and water-surface interactions (Santamaria, Das, MacDonald, & Weber, 2014).

In particular, from these works, the behaviour of the capillary pressure vs. saturation of the measured layers can be observed to be very different to that represented by the Leverett-J function in Figure 2 and Figure 3. The form of the capillary pressure vs saturation relationship as measured by (Gostick, Ioannidis, Fowler, & Pritzker, 2009) appears as follows:

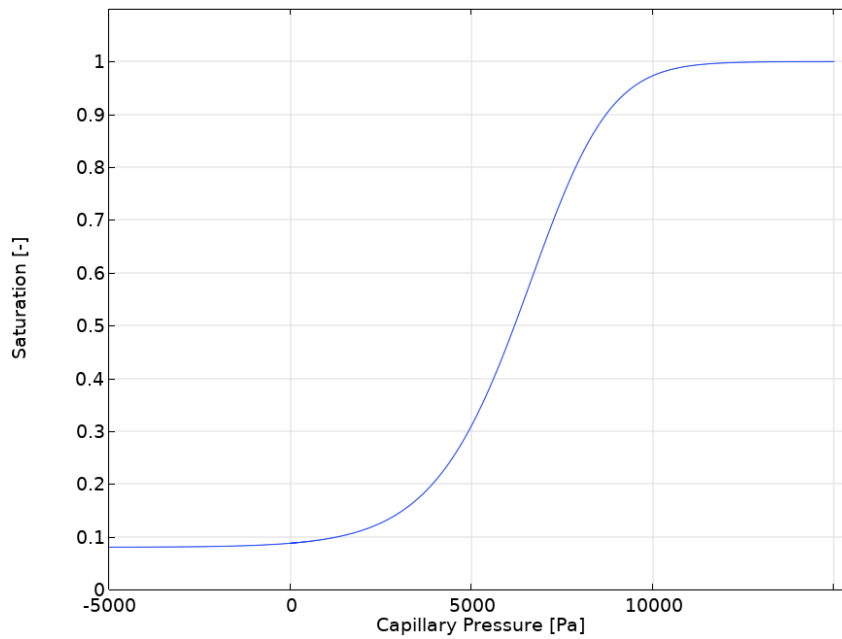


Figure 10: Saturation vs Capillary Pressure, reproduced from (Gostick, Ioannidis, Fowler, & Pritzker, 2009)

From Figure 10, it can be observed that the behaviour substantially differs from that of the Leverett-J function and would be expected to produce very different behaviour to that of the Leverett-J.

In order to implement the use of this “improved” characteristic curve, the governing equation needs to be re-formulated, re-simplified as such.

$$-\nabla \cdot \left(\frac{\rho_l k_l}{\mu_l} \nabla p_l \right) = S_l$$

The governing equation now solves for the liquid pressure locally and water moves within the MEA and other layers according to the gradient in liquid pressure as the driving force.

The characteristic transport parameter for the liquid water transport becomes the term, $\frac{\rho_l k_l}{\mu_l}$, where ρ_l and μ_l are the density of liquid water and the viscosity of liquid water, respectively – both, while function of operating conditions, are arguably constants. However, k_l is the relative liquid permeability which is related to the structure of the porous layer and the local saturation.

$$k_l = s^{N_{order}} k_{abs}$$

Where, k_{abs} is the absolute permeability and s is the saturation of the local pore volume and m is the order of the correction.

The saturation, s , is determined using the form of the relationship reported by (Gostick, Ioannidis, Fowler, & Pritzker, 2009):

$$s = s_w (s_{w,m} - s_{w,r}) + s_{w,r}$$

Where, $s_{w,m} = 1$ which is the maximum saturation of the measurement data, $s_{w,r}$ is the immobile saturation remaining after the initial intrusion. s_w is the relationship which describes the fundamental saturation vs capillary pressure relationship,

$$s_w(p_c) = 1 - \left(1 + \left(\frac{p_c + p_{atm}^{std}}{p_{c,o}} \right)^m \right)^{-n}$$

Considering this relationship, Figure 10 indicates that for a capillary pressure of 5000 [Pa] (which will be the difference in pressure between the liquid phase water and the local gas pressure) it could be expected that the layer liquid saturation would then potentially achieve a value of 0.2.

However, in reviewing the work of (Dujc, et al., 2018), they used a similar form to the one reported above and adjusted the values such that the capillary pressure achieved full saturation at a capillary pressure of approximately 70 [mbar]. The principal reason for this is due to the level of capillary pressure that builds up within the porous transport layer – which for reasonable amounts of water production in the order of several hundred millibars and (Dujc, et al., 2018) adjusted the relationship accordingly. Further consideration of Figure 10 also yields that the steepness of the curve also affects the operating saturation level (and model stability) due to the rapid rise in saturation with increasing capillary pressure – there is a very narrow zone of stability and almost a instance of flooding or drying rather than a purely stable range of running water content (from the standpoint of a steady-state model rather than a transient one).

In order to address this a study was done on values of N_{order} , it was determined that values between 4 and 6 produce capillary pressures similar to those that are observed in experiment and a value of 4.75 is initially used in this project. Based on this, the local capillary pressure in the MEA takes on the following:

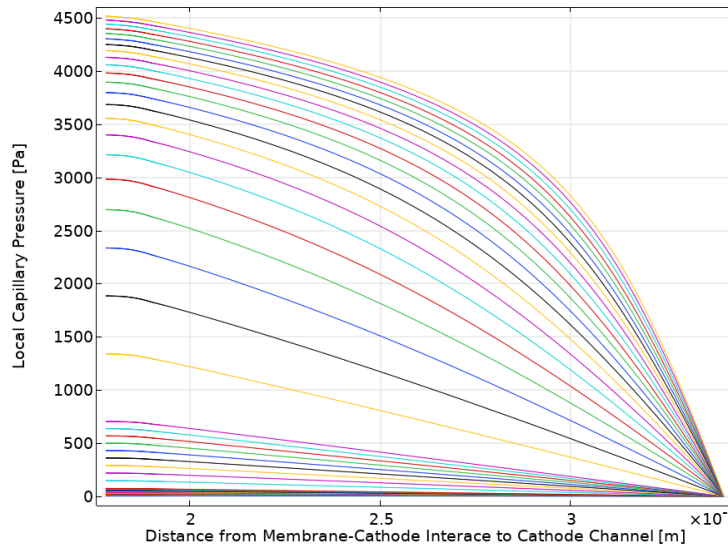


Figure 11: Capillary pressure from the membrane-cathode interface to the cathode channel interface.

From the capillary pressure in Figure 11, the local saturations in the cathode are:

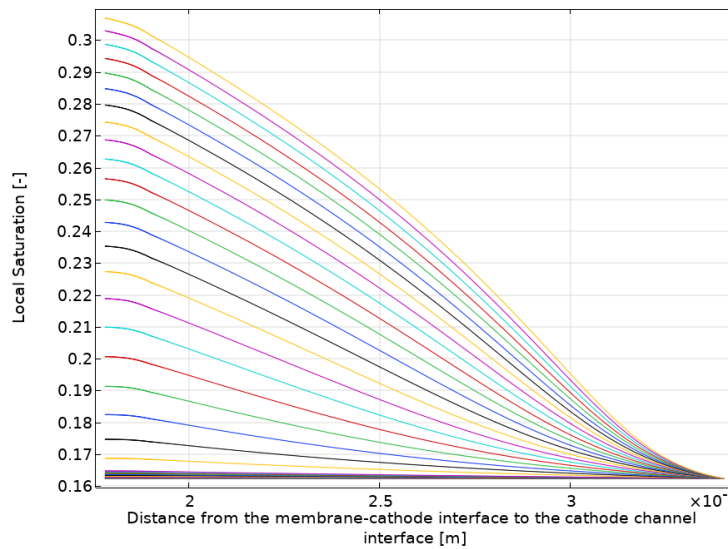


Figure 12: Local liquid saturation from the membrane-cathode interface to the cathode channel interface.

Strictly speaking, the re-formulation of the model to transport liquid water based on the liquid water pressure gradient is more thermodynamically correct than the reformulated saturation-driven approach. Further, movement away from the capillary pressure vs. saturation relationship reported by Leverett on consolidated sands to one which has been physically measured fuel cell diffusion media is also a further significant improvement. The reformulated switching terms as reported above and used in the improved ionomer water transport model are also implemented here which has further improved the model stability.

5 VERIFICATION AND VALIDATION

In order to undertake a validation of the model predictions, this process would have been done first on the liquid water transport sub-model level first. In this approach, the physics of the model could be used outside the context of a PEMFC performance prediction and be used to simulate the capillary pressure measurements used to generate the saturation vs. pressure curves. However, this data was not collected as part of Camelot and therefore the efforts will be focused on validation against experimentally collected performance data based on two conditions: Cold & Wet (NOC) and Hot and Dry. This dataset was collected by Camelot partners in WP5 and provided to WP2 to undertake the validation process.

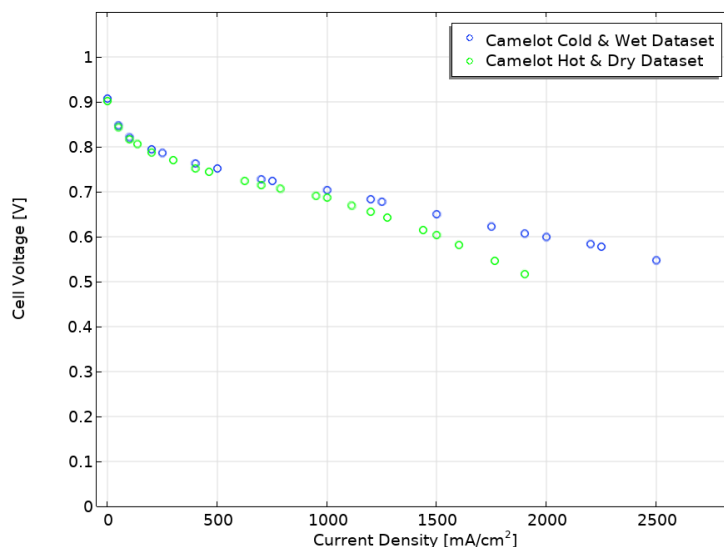


Figure 13: Validation data collected in WP5 for SoA MEAs under Cold & Wet and Hot and Dry Conditions.

The differences in the polarization data are expected to be a combination of the change in temperature and humidity and the manifestation onto the fuel cell physics. The model simulations have considered the

operating conditions, MEA structure to the extent known, and the cell hardware took the extent capturable within either a 1-D or 2-D modelling framework.

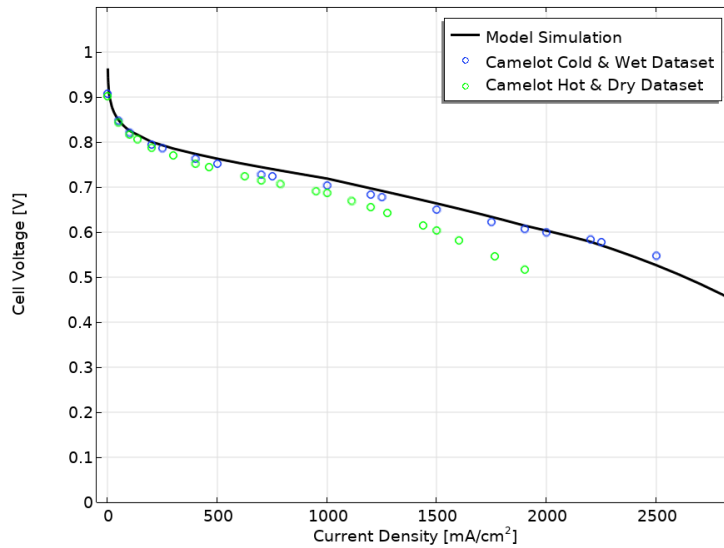


Figure 14: Performance model validation with the Cold & Wet Dataset.

The model results compare well as compared to previous simulations that did not include improved liquid water transport model or improved dissolved water transport with the updated switching. In particular, this is even more strongly observed in the Hot & Dry data set where Figure 15 shows the original comparison without the improved liquid water transport model nor the improved water transport formulation that includes the updated switching.

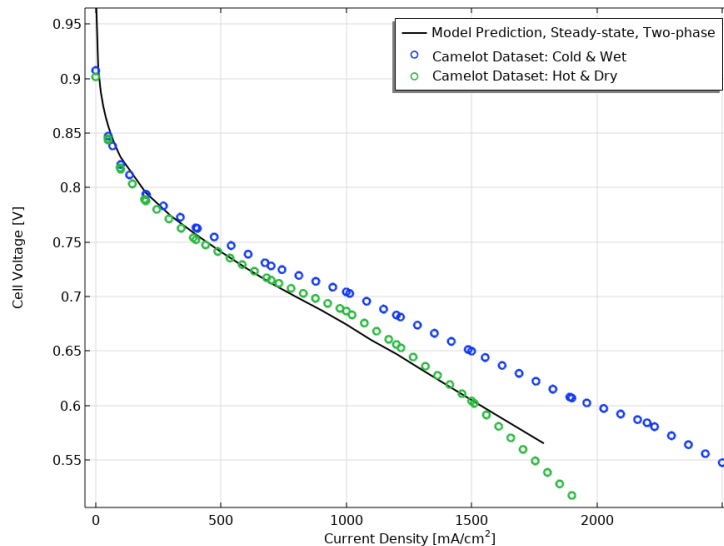


Figure 15: Previous validation attempts prior to the inclusion of the improved liquid water transport model and the updated adsorption/desorption switching process for the dissolved water transport sub-model.

With the improved sub-models, the Hot and Dry Dataset validation greatly improved in the ability of the model to capture the shape features of the polarization curve. As seen in Figure 16, the model is now beginning to be able to capture the knee that forms just after 1000 mA/cm².

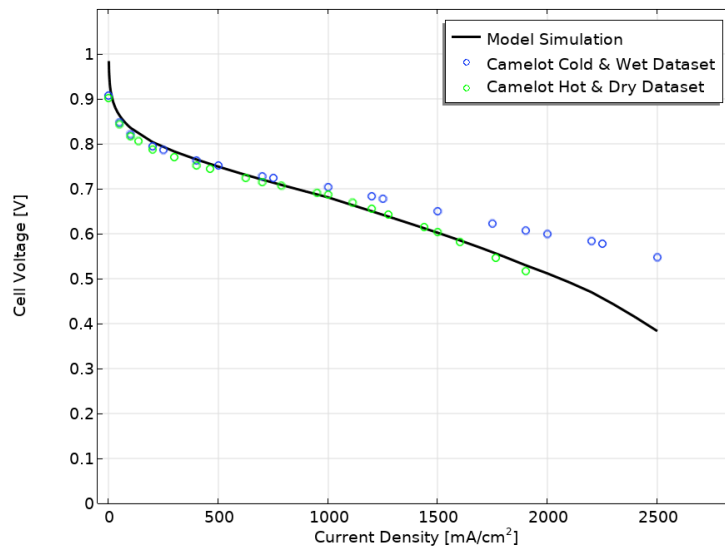


Figure 16: Performance model validation with the Hot & Dry dataset.

The characteristic that is observed between the Hot & Dry dataset and the Cold & Wet dataset, would appear to be the onset of a mass transport response. However, based on the loss breakdown and subsequent investigation has suggested that this is in fact ionomer drying. The ionomer drying creates an additional resistance loss on the anode and is caused due to the high rate of electro-osmotic drag and the inability for the anode water vapor in the gas phase to re-humidify the ionomer fast enough within the anode catalyst layer.

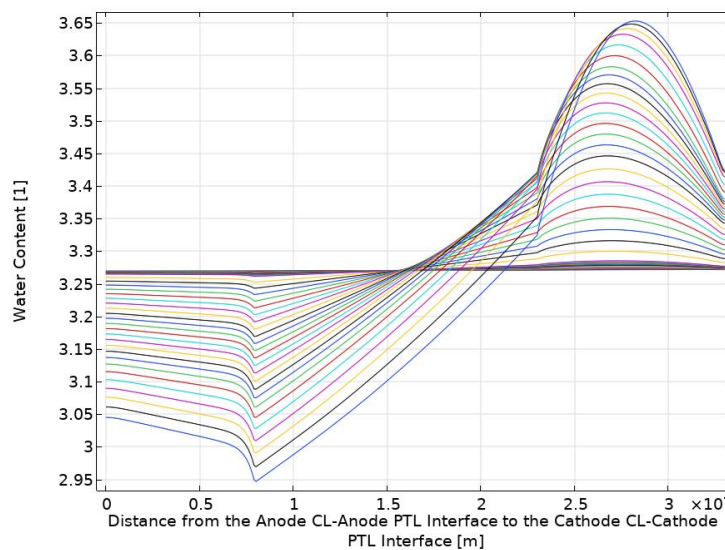


Figure 17: Water content across the CCM for the Hot and Dry Dataset.

From Figure 17, the degree of the electro-osmotic drag effect can be seen on the left of the curves where there is a steep drop across the anode catalyst layer and even more sharply drops very close to the interface with the membrane. The sharpness of the drop close to the membrane interface related to the current distribution in the anode and the fact that much of the anode current is produced in the region very close to the membrane interface. The loss due to the Hot & Dry conditions appears to arise as the anode reaction is pushed away from the interface due to the higher local resistance and is forced to move towards the GDL.

6 CONCLUSIONS AND FUTURE WORK

A revised sub-model for liquid water transport model has been implemented into FAST-FC along with further refinements and improvements in the thin ionomer dissolved water transport model. The inputs to the model will continue to require further work as much is still unknown or estimated and in the primary goal of using the model as a forward predictive tool this will need to be addressed. Additionally, as ex-situ characterization becomes available whether within the project or in the open literature it is the intent to apply the sub-models for both the pressure-driven liquid-water transport model and the thin ionomer dissolved water transport model to this ex-situ data in order to assess and separately validate the transport driving forces and transport characteristic parameters (transport parameters) further.

This model will now form the basis of the Voltage Loss Breakdown and SRU Validation as part of the project. Additionally, this model will now be applied to study the limitations of the SoA MEAs and the potential configurations for beyond-SOA MEAs.

7 REFERENCES

- A Kusoglu, A. W. (2017). New insights into perfluorinated sulfonic-acid ionomers. *Chemical Reviews*, 117(3):987–1104.
- Abriola, L. M., & Pinder, G. F. (1985). A Multiphase Approach to the Modeling of Porous Media Contamination by Organic Compounds. *Water Resources Research*, 21(1), 11-18.
- Adachi, M., Navessin, T., Xie, Z., Li, F., Tanaka, S., & Holdcroft, S. (2010). Thickness dependence of water permeation through proton exchange membranes. *Journal of Membrane Science*, 364(1):183–193.
- Atkins, P., & Paula, J. d. (2010, 9th edition). *Physical Chemistry*. Oxford University Press.
- Bear, J. (1988). *Dynamics of Fluids in Porous Media*. New York: Dover.
- Das, P. K., Li, X., & Liu, Z.-S. (2010). Analysis of liquid water transport in cathode catalyst layer of PEM fuel cells. *International Journal of Hydrogen Energy*, 35, 2403-2416.
- Dujc, J., Forner-Cuenca, A., Marmet, P., Cochet, M., Roman, V., Schumacher, J. O., & Boillat, P. (2018). Modeling the Effect of Using Gas Diffusion Layers with Patterned Wettability for Advanced Water Management in Proton Exchange Membrane Fuel Cells. *Journal of Electrochemical Energy Conversion and Storage*, 15, 1-13.
- Ge, S., Yi, B., & Ming, P. (2006). Experimental Determination of Electro-Osmotic Drag Coefficient in Nafion Membrane for Fuel Cells. *Journal of the Electrochemical Society*, 153(8), A1443 - A1450.
- Gostick, J. T., Ioannidis, M. A., Fowler, M. W., & Pritzker, M. D. (2009). Wettability and capillary behaviour of fibrous gas diffusion media for polymer electrolyte membrane fuel cells. *Journal of Power Sources*, 194, 434-444.
- Harvey, D. B. (2017). *Development of a Stochastically-driven, Forward Predictive Performance Model for PEMFCs*. Kingston: Doctoral Thesis, Queens University.
- Hwang, G., & Weber, A. Z. (2012). Effective-Diffusivity Measurement of Partially-Saturation Fuel-Cell Gas-Diffusion Layers. *Journal of The Electrochemical Society*, 159(11), F683-F692.
- Job, G., & Herrmann, F. (2006). Chemical potential – a quantity in search or recognition. *Eur. J. Phys.*, 27, 353–371.
- Karan, K. (2019). Interesting Facets of Surface, Interfacial, and Bulk Characteristics of Perfluorinated Ionomer Films. *Langmuir*, 35, 42, 13489–13520.
- Leverett, M. C. (1942). Capillary Behavior in Porous Solids. *Transactions of the AIME*, 142, 152-169.
- Motupally, A., Becker, A. J., & Weidner, J. W. (2000). Diffusion of Water in Nafion 115 Membranes. *Journal of the Electrochemical Society*, 147(9), 3171 - 3177.

- Nastarajan, D., & Nguyen, T. V. (2001). A Two-Dimensional, Two-Phase, Multicomponent, Transient Model for the Cathode of a Proton Exchange Membrane Fuel Cell Using Conventional Gas Distributors. *Journal of The Electrochemical Society*, 148(12), A1324-A1335.
- Santamaria, A. D., Das, P. K., MacDonald, J. C., & Weber, A. Z. (2014). Liquid-Water Interactions with Gas-Diffusion-Layer Surfaces. *Journal of The Electrochemical Society*, 161(2), F1184-F1193.
- Shah, A., Kim, G., Sui, P., & Harvey, D. (2007). Transient non-isothermal model of a polymer electrolyte fuel cell. *Journal of Power Sources*, 163(2) Pages 793-806.
- Shimoaka, T., Wakai, C., Sakabe, T., Yamazaki, S., & Hasegawa, T. (2015). Hydration structure of strongly bound water on the sulfonic acid group in a Nafion membrane studied by infrared spectroscopy and quantum chemical calculation. *Physical Chemistry Chemical Physics*, 17, 8843-8849.
- Springer, T., Zawodsinski, T., & Gottesfeld, S. (1991). Polymer electrolyte fuel cell model. *Journal of the Electrochemical Society*, 138(8):2334 – 2342.
- Takata, H., Mizuno, N., Nishikawa, M., Fukada, S., & Yoshitake, M. (2007). Adsorption properties of water vapor on sulfonated perfluoropolymer membranes. *International Journal of Hydrogen Energy*, 32(3) 371-379.
- Udell, K. S. (1985). Heat transfer in porous media considering phase change and capillarity - the heat pipe effect. *International Journal of Heat and Mass Transfer*, 28(2), 485-495.
- Vetter, R., & Schumacher, J. O. (2019). Experimental parameter uncertainty in proton exchange membrane fuel cell modeling. Part I: Scatter in material parameterization. *Journal of Power Sources*, 438, 227018. doi:10.1016/j.jpowsour.2019.227018
- Vetter, R., & Schumacher, J. O. (2019). Free open reference implementation of a two-phase pem fuel cell model. *Computer Physics Communications*, 234, 223–234.
- Wagner, W., & Pruß, A. (2002). The IAPWS Formulation 1995 for the Thermodynamic Properties of Ordinary Water Substance for General and Scientific Use. *Journal of Physical and Reference Chemical Data*, 31(2) 387.
- Wang, C., & Cheng, P. (1996). A multiphase mixture model for multiphase, multicomponent transport in capillary porous media - I. Model development. *International Journal of Heat and Mass Transfer*, 39(17), 3607-3618.
- Wang, Y., & Wang, C.-Y. (2006). A Nonisothermal, Two-Phase Model for Polymer Electrolyte Fuel Cells. *Journal of The Electrochemical Society*, 153(6), A1193-A1200.
- Weber, A. Z. (2010). Improved modeling and understanding of diffusion-media wettability on polymer-electrolyte-fuel-cell performance. *Journal of Power Sources*, 195, 5292-5304.
- Weber, A., & Newman, J. (2004). Transport in polymer-electrolyte membranes ii. Mathematical model. *Journal of The Electrochemical Society*, 151(2):A311–A325.

This project has received funding from the Fuel Cells and Hydrogen 2 Joint Undertaking (now Clean Hydrogen Partnership) under grant agreement No 875155. This Joint Undertaking receives support from the European Union's Horizon 2020 Research and Innovation program, Hydrogen Europe and Hydrogen Europe Research.

